MR Multitasking for Multi-dimensional Assessment of Cardiovascular System (MT-MACS): Development and Feasibility Study on the Thoracic Aorta

Zhehao Hu[1,2], **Anthony G. Christodoulou**[1,3], **Nan Wang**[1,2], **Jaime L. Shaw**[1], **Shlee S. Song**[4], **Marcel M. Maya**[5], **Mariko L. Ishimori**[6], **Lindsy J. Forbess**[6], **Jiayu Xiao**[1], **Xiaoming Bi**[7], **Fei Han**[7], **Debiao Li**[1,2,3], **Zhaoyang Fan**[1,2,3,*]

[1]Biomedical Imaging Research Institute, Cedars-Sinai Medical Center, Los Angeles, California

[2]Department of Bioengineering, University of California, Los Angeles, California

[3]Department of Medicine, University of California, Los Angeles, California

[4]Department of Neurology, Cedars-Sinai Medical Center, Los Angeles, California

[5]Department of Imaging, Cedars-Sinai Medical Center, Los Angeles, California

[6]Department of Rheumatology, Cedars-Sinai Medical Center, Los Angeles, California

[7]Siemens Healthcare, Los Angeles, California

Abstract

Purpose: To develop an MR MultiTasking (MT) based Multi-dimensional Assessment of Cardiovascular System (MACS) with ECG- and navigator-free data acquisition for a comprehensive evaluation of thoracic aortic diseases.

Methods: MT-MACS adopts a low-rank tensor image model with a cardiac time dimension for phase-resolved cine imaging and a T2-prepared inversion recovery dimension for multi-contrast assessment. Twelve healthy subjects and two patients with thoracic aortic diseases were recruited for the study at 3T, and both qualitative (image quality score) and quantitative (contrast-to-noise ratio [CNR] between lumen and wall, lumen [LA] and wall area [WA], aortic strain index) analyses were performed in all healthy subjects. The overall image quality was scored based on a 4-point scale: 3-excellent, 2-good, 1-fair and 0-poor. Statistical analysis was used to test the measurement agreement between MT-MACS and their corresponding 2D references.

Results: MT-MACS images reconstructed from acquisitions as short as 6 minutes demonstrated good or excellent image quality for bright-blood (2.58±0.46), dark-blood (2.58±0.50) and gray-blood (2.17±0.53) contrast weightings, respectively. The CNRs for the three weightings were 49.2±12.8, 20.0±5.8 and 2.8±1.8, respectively. There were good agreements in the lumen and wall area (intraclass correlation coefficient [ICC]=0.993, P<0.001 for LA; ICC=0.969, P<0.001 for WA) and strain (ICC=0.947, P<0.001) between MT-MACS and conventional 2D sequences.

*Correspondence to: Zhaoyang Fan, PhD, Biomedical Imaging Research Institute, Cedars-Sinai Medical Center, 8700 Beverly Blvd., PACT Suite 400.7O, Los Angeles, CA 90048, Zhaoyang.Fan@cshs.org.

Conclusion: MT-MACS provides high-quality, multi-dimensional images for a comprehensive assessment of the thoracic aorta. Technical feasibility was demonstrated in healthy subjects and patients with thoracic aortic diseases. Further clinical validation is warranted.

Keywords

thoracic aorta; MR multitasking; multi-contrast imaging; phase-resolved imaging

---

1. Introduction

Thoracic aortic diseases are one of the most common causes of cardiovascular morbidity and mortality, and could end in potentially calamitous consequences (1,2). For example, vulnerable atherosclerotic plaques at the aortic arch are considered a major embolic source for ischemic stroke (3), and aortic aneurysms increase the risk of aortic wall rupture and internal bleeding. Unfortunately, patients with aortic diseases usually have no signs or symptoms and are unaware of the pathological changes in their aortas before adverse events occur (4). Thus, diagnosis and follow-up of aortic abnormalities depend exclusively on diagnostic imaging (5).

Several imaging modalities are traditionally used for thoracic aortic disease assessment in clinical practice. Transesophageal echocardiography (TEE) provides high-quality imaging of the thoracic aorta because of the use of high-frequency transducers and the close proximity of the esophagus to the aorta (2). However, this modality is invasive and introduces considerable discomfort to patients, and not all parts of the thoracic aorta can be visualized due to a limited field of view (6). Computed tomography (CT) angiography is currently the most widely used diagnostic modality due to its near universal availability and rapid acquisition (7,8). However, CT angiography focuses on the detection of luminal abnormalities while providing limited information on pathological changes within the aortic vessel wall (9). In addition, CT angiography may be contraindicated in certain population due to the concerns about exposure to ionizing radiation or allergic reaction to iodinated contrast material (10). Magnetic resonance (MR) has emerged as a radiation-free, noninvasive imaging modality for diagnosing thoracic aortic diseases (8). The most common MR approach is MR angiography that can be achieved by exploiting either contrast-enhanced (i.e. CE-MRA) (11,12) or non-contrast (i.e. time-of-flight [TOF] and steady state free precession [SSFP]) (13–15) technologies. However, as another type of lumenography-based imaging modality, MR angiography shares with CT angiography the same limitation in lumen-only imaging.

The clinical potential of MR for the assessment of thoracic aortic diseases is being advanced with continued technical developments over the last decade. MR vessel wall imaging, primarily based on the dark-blood contrast weighting, has been proposed as a useful tool for directly evaluating vessel wall characteristics (i.e. thickened, remodeled or inflammatory status) (16,17). More recently, MR vessel wall imaging evolved from single, dark-blood contrast to multi-contrast approaches to facilitate the characterization of vulnerable atherosclerotic plaque components or to provide a more comprehensive disease assessment. Several recently developed three-dimensional (3D) techniques tailored to thoracic aorta

acquire different image contrasts through separate scans (9,18). MR cine imaging is another technique proposed for evaluating aortic wall functions such as vessel compliance. Abnormal compliance (or strain index) has been shown to be implicated in pathogenesis of aortic aneurysm and dissection (19,20). Despite the prominent features and clinical necessities, adoption of a comprehensive protocol is hindered by three typical limitations: (a) long acquisition time associated with the need for large spatial coverage and high spatial resolution; (b) image misregistration due to subject motion among multiple scans; (c) nontrivial imaging setup and sacrifice of efficiency for addressing motion during data acquisition, such as electrocardiography (ECG) triggering and respiratory navigator gating or breath-holding, which is a particular problem for patients with cardiac arrhythmias or difficulty in holding their breath.

MR multitasking is a recently proposed imaging framework that can address several longstanding problems in cardiovascular MR imaging (21). Instead of applying conventional motion-compensation strategies, which constrain data acquisition periodically in a predefined time window to minimize physiological motion and ensure a specific contrast weighting, MR multitasking allows continuous data acquisition and retrospectively resolves different dynamics (i.e. physiological motion, physical relaxation), making it possible to acquire multiple co-registered images in one single scan with no reliance on triggering signals. Furthermore, by adopting a low-rank tensor (LRT) image model which exploits the high correlation between images at different time points, MR multitasking bypasses the "curse of dimensionality" and thereby allows expedited acquisitions (21,22).

Because of the crucial role imaging plays in the diagnosis of thoracic aortic diseases and longstanding challenges of conventional imaging modalities, in this work, we developed an MR MultiTasking (MT) based 3D Multi-dimensional Assessment of Cardiovascular System (MACS) technique for comprehensive thoracic aortic vessel imaging. Without the use of ECG and respiratory navigators, this technique allows for motion-resolved, isotropic high-spatial-resolution, multi-dimensional (multiple contrast weightings and cine images) imaging of the thoracic aorta within 6 minutes. Technical feasibility was demonstrated in healthy volunteers and patients with thoracic aortic diseases.

2. Methods

2.1 Multidimensional Imaging based on MR Multitasking

The proposed MT-MACS method uses an LRT image model with a cardiac time dimension for phase-resolved cine imaging, and a T2-prepared inversion recovery dimension for multi-contrast (i.e. bright-blood [BB], dark-blood [DB], and gray-blood [GB]) assessment. Specifically, MT-MACS models a 6-dimensional aortic image as a 4-way multidimensional array (or "tensor") $\mathscr{I}$, with one dimension indexing 3D spatial location $\mathbf{x}$ and three time dimensions: cardiac motion t_c, respiration t_r and inversion recovery t_{T1}. The strong correlation between aortic images along and across time dimensions makes $\mathscr{I}$ a low-rank tensor, and therefore partially separable in the following sense (23):

$$\mathcal{I}(\mathbf{x}, t_{\mathrm{c}}, t_{\mathrm{r}}, t_{\mathrm{T1}}) = \sum_{\ell=1}^{L} u_{\ell}(\mathbf{x})\phi_{\ell}(t_{\mathrm{c}}, t_{\mathrm{r}}, t_{\mathrm{T1}}) \tag{1}$$

where $u_{\ell}(\mathbf{x})$ is the ℓth of L basis images and $\phi_{\ell}(t_{\mathrm{c}}, t_{\mathrm{r}}, t_{\mathrm{T1}})$ is the ℓth of L temporal functions. Furthermore, in the LRT image model, each $\phi_{\ell}(t_{\mathrm{c}}, t_{\mathrm{r}}, t_{\mathrm{T1}})$ is itself low-rank and can be factorized by using individual bases for each time dimension:

$$\phi_{\ell}(t_{\mathrm{c}}, t_{\mathrm{r}}, t_{\mathrm{T1}}) = \sum_{m=1}^{M} \sum_{n=1}^{N} \sum_{p=1}^{P} c_{\ell mnp} v_m(t_{\mathrm{c}}) w_n(t_{\mathrm{r}}) z_p(t_{\mathrm{T1}}) \tag{2}$$

where v, w and z denote basis functions along the cardiac motion, respiration and inversion recovery dimensions, respectively, and $c_{\ell mnp}$ are elements of the core tensor $\mathcal{C}$. Thus, our image tensor $\mathcal{I}$ can be expressed in matrix form as:

$$\mathbf{I}_{(1)} = \mathbf{U_x}\mathbf{C}_{(1)}(\mathbf{Z}_{t_{\mathrm{T1}}} \otimes \mathbf{W}_{t_{\mathrm{r}}} \otimes \mathbf{V}_{t_{\mathrm{c}}})^T \tag{3}$$

where $\mathbf{I}_{(1)}$ denotes mode-1 unfolding of the tensor $\mathcal{I}$ into a matrix, the factor matrix $\mathbf{U_x}$ contains basis images, $\mathbf{C}_{(1)}$ denotes the unfolded core tensor, and $\mathbf{V}_{t_{\mathrm{c}}}, \mathbf{W}_{t_{\mathrm{r}}}$ and $\mathbf{Z}_{t_{\mathrm{T1}}}$ contain temporal basis functions for each time dimension. The $\otimes$ operator denotes the Kronecker product (24). Currently, there are various low-rank strategies available for reconstruction of the multidimensional arrays, either implicitly or explicitly (21,25–29). MR multitasking, based on the description of previous works (21,22,30,31), uses a mixed strategy which reconstructs the image tensor by directly recovering each of its factor matrices. Basically, in this work, image reconstruction can be divided into 5 steps:

1. Generate ungated images, which are reconstructed using explicit low-rank matrix imaging with only one time dimension representing elapsed time (21,22), for image-based cardiac phase and respiratory position identification by means of a modified T1 recovery aware k-means clustering approach (21), placing the corresponding images into 14 cardiac bins and 6 respiratory bins.

2. Pre-determine the temporal basis functions in $\mathbf{Z}_{t_{\mathrm{T1}}}$ (along the inversion recovery dimension) from a training dictionary of inversion recovery signals with different T1, T2, B1 inhomogeneity values, which is generated according to the Bloch equations ahead of time (21,31).

3. Apply small-scale LRT completion to recover missing elements from a frequently sampled subset of k-space ("auxiliary data"), which will be undersampled since it is impossible to acquire every combination of cardiac phase, respiratory phase and inversion recovery time point:

$$\widehat{\mathcal{D}}_{\mathrm{aux}} = arg \min_{\mathcal{D}_{\mathrm{aux}} \in \mathrm{range}(\mathbf{Z}_{t_{\mathrm{T1}}})} \|\mathbf{d}_{\mathrm{aux}} - \Omega(\mathcal{D}_{\mathrm{aux}})\|_2^2 + \lambda \sum_{n=1}^{4} \|\mathbf{D}_{\mathrm{aux},(n)}\|_* \tag{4}$$

where $\mathbf{d}_{aux}$ is the collected auxiliary data, $\Omega(\cdot)$ represents the undersampling pattern of the auxiliary dataset, $\mathbf{D}_{aux,(n)}$ denotes the mode-n flattening of the completed auxiliary tensor, and $\|\cdot\|_*$ is the nuclear norm which promotes low-rankness of each unfolded matrix.

4. Truncate the high-order SVD of $\widehat{\mathbf{D}}_{aux,(1)}$ to recover $\mathscr{C}$ and the temporal basis functions along the cardiac and respiratory phase directions, namely $\mathbf{V}_{t_c}$ and $\mathbf{W}_{t_r}$, respectively.

5. Solve the following optimization problem to reconstruct the spatial coefficients $\mathbf{U_x}$:

$$\widehat{\mathbf{U}_\mathbf{x}} = arg\min_{\mathbf{U_x}}\|\mathbf{d} - \Omega[\mathbf{FSU_x}\cdot\mathbf{C}_{(1)}\big(\mathbf{Z}_{t_{T1}}\bigotimes\mathbf{W}_{t_r}\bigotimes\mathbf{V}_{t_c}\big)^T]\|_2^2 + \lambda R(\mathbf{U_x}) \qquad (5)$$

where $\mathbf{d}$ is the acquired imaging data, $\mathbf{F}$ applies Fourier transform, and $\mathbf{S}$ applies coil sensitivity maps. The regularization functional $R(\cdot)$ here is chosen as a spatial wavelet sparsity penalty, and λ is the parameter used to balance between wavelet sparsity and noise artifacts. The MATLAB (R2018a, MathWorks, Natick, MA) p-code for the reconstruction is available upon request.

2.2 Pulse Sequence Design

The MT-MACS technique was implemented based on a prototype free-running fast low-angle shot (FLASH) Cartesian acquisition immediately following intermittent T2-inversion recovery (T2-IR) magnetization preparation (Figure 1). The T2-IR preparative module was used to leverage T1 and T2 variances to (a) maximize the contrast between the vessel wall and blood, and (b) create multiple image contrasts (32,33). After the FLASH readouts, a short gap of fixed duration allows T1 recovery towards thermal equilibrium. Both phase and partition encodings for the imaging data $\mathbf{d}$ were collected with randomized ordering according to a variable-density Gaussian distribution, in order to achieve incoherent undersampling of the k-space (30,31). The auxiliary data $\mathbf{d}_{aux}$ collected at the center k-space ($k_y=k_z=0$) was interleaved with the imaging data every 9 readouts. This ensured an auxiliary data sampling interval of 40 ms, which is adequate for capturing our targeted dynamic processes without sacrificing total imaging data. Too infrequent collection of auxiliary data cannot capture the overlapping dynamic processes while too frequent collection comes at the cost of fewer imaging data, which would lead to degradation of the final image quality.

2.3 Simulation

To maximize the lumen-wall contrast, a simulation study was performed to optimize two parameters: (a) repetition time (TR), which is the time interval between two consecutive T2-IR preparation pulses; (b) number of readout segments within each TR. The simulation study was conducted in two steps. We first assumed readouts were continuous acquired every 4.5 ms (a practically achievable echo spacing) throughout the entirety of each TR. The curve of lumen-wall contrast against various TRs (Figure 2A) illustrates that short TRs would not provide adequate signal contrast between the vessel wall and blood. On the other hand, long TRs may not be SNR efficient, as the magnetization will spend too much time in

the steady-state rather than near the desired image contrasts. Therefore, a 2000-ms TR was empirically chosen here (Figure 2B) as a compromise. With the TR fixed, Figure 2C illustrates the lumen-wall contrast against the number of segments in each TR. Too many segments lead to less contrast; however, too few segments lead to a longer gap, reducing data acquisition efficiency and potentially degrading final image quality for a fixed total scan time. Based on simulations and several pilot in-vivo experiments, we used 300 readout segments (approximately 1400 ms) followed by a 600-ms gap within each TR (Figure 2D). For the simulation purpose, the segment for which the vessel wall signal reached the nulling point was selected for the BB contrast, and the time point when the signal of lumen blood reached the nulling point was chosen for the DB contrast. The relevant imaging parameters used in simulations were: T1 = 1412 ms and T2 = 50 ms for vessel wall, T1 = 1932 ms and T2 = 275 ms for lumen blood, flip angle = 8°, echo spacing = 4.5 ms, duration of T2-IR preparation module = 60 ms.

2.4   In vivo Study

The in vivo study was approved by the local institutional review board and all subjects provided written informed consent before participation. Twelve healthy volunteers (aged 18–63 years, 7 females) and two patients (aged 38–71 years, 2 females) with aortic atherosclerosis and aortic aneurysm, were recruited for the study. All imaging examinations were performed on a 3T clinical MR scanner (MAGNETOM Skyra; Siemens Healthcare, Erlangen, Germany) with a standard 18-channel body coil and an integrated spine matrix coil.

In all healthy volunteers, MT-MACS imaging was performed with no ECG and respiratory navigator in an oblique sagittal orientation as determined using the three-point tool on localizer images. Major imaging parameters included: field of view (FOV) = 275×220×72 mm, matrix size = 200×160, number of slices = 52, spatial resolution = 1.38 mm isotropic, flip angle = 8°, TR/TE = 2000.0/2.1 ms, echo spacing = 4.5 ms, bandwidth = 1008 Hz/pixel, and 1–2-1 binomial-pulse spectrally selective water excitation for fat suppression. Imaging time was set 10 minutes and the acquired data later underwent offline reconstruction with different k-space raw data truncations corresponding to 4, 6, 8, 10 min scan durations for the goal of scan time optimization. MT-MACS imaging with 6-minute scan time (as optimized in the healthy volunteers) was performed on the two patients.

In addition, conventional sequences were also acquired in 9 out of the 12 healthy subjects to serve as the references for morphological (i.e. lumen and wall area) and functional (i.e. strain index) quantification of the thoracic aorta. Briefly, 2D T1-weighted dark-blood vessel wall imaging based on double inversion recovery prepared turbo spin-echo (TSE) sequence and 2D cine imaging based on the balanced steady-state free precession (bSSFP) sequence were performed at both the ascending and descending thoracic aorta, with ECG-triggering and end-expiration breath-holding. Major imaging parameters for 2D TSE sequence included: FOV = 350×285 mm, matrix size = 256×208, slice thickness = 5 mm, flip angle = 180°, TR = 1 cardiac cycle, TE = 27 ms, turbo factor = 12, echo spacing = 5.49 ms, bandwidth = 849 Hz/pixel, and ECG-triggered to the mid-diastole. Three contiguous slices were acquired with the purpose of reducing the measurement errors of vessel morphology

induced by position-mismatch between MT-MACS and 2D TSE sequence. For 2D cine imaging, protocol parameters included: FOV = 350×285 mm, matrix size = 256×208, slice thickness = 6 mm, flip angle = 50°, TR/TE = 45.9/2.5 ms, echo spacing = 3.3 ms, bandwidth = 962 Hz/pixel, and 25 phases based on retrospective gating.

2.5 Image Analysis

Images acquired using the MT-MACS technique were reconstructed offline and generated in a DICOM format using MATLAB. These DICOM images were loaded to a workstation (LEONARDO, Siemens Healthcare) for the following analysis.

2.5.1 Qualitative analysis—

For each healthy subject, four groups of multi-contrast mid-diastolic end-expiratory images were reconstructed using different amounts of MT-MACS k-space raw data corresponding to 10, 8, 6, 4-minute long acquisitions, respectively. Three inversion recovery time points were chosen to provide BB, DB, and GB image contrasts. All the MT-MACS image sets were randomized and evaluated by two independent radiologists with at least 5 years of experience in cardiovascular imaging. Overall image quality was graded using a 4-point scale: 0-poor, unidentifiable and completely blurred lumen and wall; 1-fair, identifiable but heavily blurred lumen and wall; 2-good, well-defined lumen and wall with slight artifacts; 3-excellent, excellent visualization and sharp vessel wall and lumen margins with no artifacts. The final image quality score was determined as an average between the two readers. Optimal scan time was determined as the shortest one that generated average scores of 2 over all subjects for each image contrast.

2.5.2 Quantitative analysis—

Quantitative analysis was performed on the MT-MACS images reconstructed using the data acquired within the scan time optimized above. Contrast-to-noise ratio (CNR) of the vessel wall versus lumen blood was determined from all the three image contrasts at the mid-diastolic end-expiratory phase using the following equation

$$CNR = \frac{|SI_{LB} - SI_{VW}|}{\sigma_{BG}} \tag{6}$$

where SI_{LB} and SI_{VW} represent the mean signal intensity of the lumen blood and the vessel wall, respectively, within three regions-of-interest located at the ascending aorta (AAo), aortic arch (AoA) and descending aorta (DAo), and σ_{BG} is the standard deviation of signal intensities in a neighboring artifact-free air region.

For the accuracy analysis of lumen area (LA) and wall area (WA) measurements, the DB images of MT-MACS at the mid-diastolic end-expiratory phase were reformatted to match the 2D dark-blood TSE images in both location and slice thickness. Inner and outer boundaries of the vessel wall on all cross-sectional slices acquired by each of the two sequences were manually traced by a radiologist. Based on these contours, the LA and WA of both the AAo and DAo were measured. Mean LA and WA values of each healthy subject were obtained by averaging the measurement results of the three contiguous slices.

For the accuracy analysis of the strain index measurement, cardiac phase-resolved BB images of MT-MACS were reconstructed and reformatted to match cine bSSFP images in both location and slice thickness. The strain index was measured for each of the two sequences using the following equation (34)

$$Strain = \frac{(SA - DA)}{DA} \tag{7}$$

where *SA* was the maximal systolic lumen area and *DA* was the minimal diastolic lumen area of the aorta. The lumen area was determined after manually contouring the lumen by a radiologist.

2.6 Statistical Analysis

Linear regression and intraclass correlation coefficients (ICC) were used to test measurement agreement in morphological and functional parameters obtained from MT-MACS images and their corresponding 2D reference sequences. The measurement differences were also compared using Bland-Altman analysis. A P value < 0.05 was considered to indicate statistical significance. All statistical analysis was performed using OriginPro (version 9.1, Northampton, Massachusetts, USA).

3. Results

MT-MACS imaging was performed successfully on all 12 healthy subjects and 2 patients with thoracic aortic diseases. Figure 3 is the illustration of multiple time dimensions for the MT-MACS technique and some example images resulting from the multidimensional image reconstruction. 6 respiratory phases lie along the respiratory time axis (vertical), 14 cardiac phases lie along the cardiac time axis (depth) and 300 inversion recovery segments lie along the T1 recovery time axis (horizontal). Three representative time points were picked out among the 300 segments for BB, DB and GB imaging, respectively. Supporting Information Video S1 – S6 demonstrate the cardiac and respiratory motion with all these three selected image contrast weightings.

3.1 Qualitative Analysis

A total of 144 (3 image contrasts × 4 data amounts × 12 subjects) 3D image sets were scored for image quality. Figure 4 shows the average image quality scores and corresponding standard deviations over all subjects for each image contrast within each scan time category (**A**) and representative images (**B**). For BB MT-MACS images, the image quality scores for 10-minute, 8-minute, 6-minute and 4-minute datasets were 3.00±0.00, 2.83±0.33, 2.58±0.46, and 1.58±0.46, respectively; for DB MT-MACS images, the image quality scores were 2.96±0.14, 2.92±0.19, 2.58±0.50, and 2.08±0.63, respectively; for MT-MACS GB images, the image quality scores were 2.71±0.45, 2.5±0.71, 2.17±0.53, and 1.58±0.70, respectively. Scans in as short as 6 minutes provided good or excellent image quality with moderate-to-high inter-reader agreement quantified by weighted Cohen's kappa (κ) values 0.667 (P = 0.014), 1.000 (P < 0.001) and 0.739 (P < 0.001) for BB, DB and GB imaging, respectively (image quality scores given by both readers were shown in Supporting Information Table S1 and Supporting Information Figure S1). Thus, the 6-minute image sets were chosen for the

following quantitative analysis. Some example images for all three image contrasts according with each image quality score were displayed in the Supporting Information Figure S2.

3.2 Quantitative Analysis

The CNR measurements for BB, DB and GB contrast weightings are 49.2±12.8, 20.0±5.8, and 2.8±1.8, respectively, which are in line with the values published in the literature (16,35,36).

Comparison of measurements for several morphological parameters, including the LA and WA for both the AAo and DAo, is shown in Figure 5A. In Figure 5B and 5D, linear regression analyses demonstrated excellent intraclass correlation between two imaging techniques (ICC = 0.993, P < 0.001 for LA; ICC = 0.969, P < 0.001 for WA), with slopes and ordinate intercepts of approximately one (range: 0.97 – 1.00) and zero (range: −0.08 – 0.00 cm^2), respectively. According to Bland-Altman plots (Figure 5C, 5E), excellent agreements of both LA and WA measurement results were observed between MT-MACS and 2D dark-blood TSE image sets. For LA measurements, there was an absolute mean difference of 0.067 with 95% limits of agreement from −0.234 to 0.368 (N = 18 slices); for WA measurements, the absolute mean difference was 0.058 with 95% limits of agreement from −0.119 to 0.235 (N = 18 slices).

Comparison of aortic vessel strain index measurements between MT-MACS and 2D cine bSSFP is displayed in Figure 6. Good agreement was observed between these two techniques (mean: 3.1%; 95% limits of agreement: −5.0% to 11.1%; N = 18 slices). The regression analysis illustrated a good linear relation (R^2 = 0.890, P < 0.001) and correlation (ICC = 0.947, P < 0.001) between measurements.

3.3 Detection of Aortic Abnormalities

Figure 7A, 7B and 7C show bright-blood, dark-blood and gray-blood contrasts, respectively, acquired by MT-MACS sequence from a 38-year-old female patient with aortic aneurysm. Aneurysm affecting the patient's descending aorta was clearly depicted in all three image contrasts (red boxes). Moreover, through gray-blood imaging, calcified spots, which were pointed out by yellow arrowheads, were identified. The circumferential extent of the abnormalities could be better understood through reformatted short-axis views (yellow arrowheads).

Figure 7D, 7E and 7F are imaging results of a 71-year-old female patient with aortic atherosclerosis. Wall thickness at the descending aorta was 4.491 mm (marked out in red on the oblique sagittal DB image), which is much higher than that of healthy subjects (approximately 2 mm). The increase of aortic vessel wall thickness could be confidently identified through the short-axis views of DB and GB image contrasts (pointed out by the yellow arrows), which suggested the existence of aortic atherosclerosis.

4. Discussion

In this study, we presented a novel ECG- and navigator-free 3D MT-MACS technique and demonstrated its feasibility on the thoracic aorta in healthy subjects and patients with thoracic aortic diseases. The proposed MT-MACS achieved high spatial resolution with complete thoracic aorta coverage, and more importantly, provided a comprehensive assessment (multiple image contrasts and cine imaging) of the thoracic aorta within a single 6-minute scan.

Thoracic aortic disease is a stealth condition, which develops silently and typically without any symptoms, but the catastrophic results could affect people at any age (1). Therefore, imaging plays a crucial role in the monitoring and treatment planning of different types of aortic diseases (8). Given the abundant strengths of MR imaging over other imaging modalities, in this work, MT-MACS was developed to provide a comprehensive assessment of the thoracic aorta. Compared with previous MR imaging techniques tailored for the thoracic aorta, the proposed method has several advantages. Firstly, MT-MACS provides multiple co-registered images with different image contrast weightings in a single 6-minute scan. To date, MR angiography, including both contrast enhanced (CE-MRA) and unenhanced (SSFP, TOF) technique, has been increasingly favored by clinicians and radiologists in the assessment of thoracic aortic diseases (11,14). However, characterizing aortic diseases by simply visualizing the aortic lumen may underestimate the vulnerability and severity of diseases under certain pathological circumstances (i.e. positive remodeling effects in the development of aortic atherosclerosis) (9,37). Therefore, many MR multi-contrast aortic imaging studies were performed with the purpose of directly visualizing the aortic vessel wall and major plaque components, such as intra-plaque hemorrhage and calcification (9,38). Yet, the long acquisition time (about 30 – 40 min) and misregistration due to inter-scan subject motion rendered multi-contrast imaging logistically unpractical and complicated to interpret (18). In this work, we adopted a T2-prepared inversion recovery (T2-IR) module to maximize the contrast between the aortic vessel wall and lumen blood and acquired different image contrasts by retrospectively selecting images at different time points along the T1 recovery time dimension. More specifically, there were 300 readout segments within each inversion recovery period and thus 300 different image contrasts were available through this sequence. Three typical image contrasts out of 300 were picked out, namely bright-blood, dark-blood and gray-blood image contrasts. BB images had significantly high signal in the aortic lumen and can be used to detect lumen abnormalities, such as luminal stenosis. The second image contrast, DB images, with suppressed blood signal and higher signal in the aortic vessel wall, can be used to directly visualize the wall morphology. The third image contrast, GB images, which had similar signal levels in the lumen and wall, is designed specifically for the detection of CA, especially the superficial calcified nodules (36,39). However, dark-blood image contrast may not ideally identify the vessel wall boundary due to the insufficient contrast between vessel wall and surrounding tissues. As a technical advantage, MT-MACS can provide sliding contrasts to help better delineate aortic wall boundaries (Supporting Information Video S7). With all these co-registered image contrasts acquired within the same scan, we can greatly simplify the acquisition workflow and improve the interpretation efficiency and accuracy.

Secondly, by adopting the MR multitasking framework, the acquisition eliminates the need for ECG triggering, respiratory navigators or breath-holds. For aortocardiac imaging, one of the major challenges is to perform imaging in the presence of physiological movement, i.e. cardiac pulsation and respiration. Conventional cardiovascular MR imaging techniques adopt ECG for triggering data acquisition to a quiescent cardiac phase (usually mid-diastole) and breath-holding or navigator gating with a low-rate acceptance window to resolve respiratory motion, thus leading to dramatically inefficient imaging. Furthermore, these unreliable (i.e. ECG-triggering at 3 Tesla) or uncomfortable (i.e. breath-holding) motion resolving strategies may result in severe motion artifacts for specific subjects, for example, patients with cardiac arrhythmias (21). The presented work could potentially overcome the abovementioned problems by developing an ECG- and navigator-free imaging technique adapted from the MR multitasking framework. By a single simple-setup scan, the proposed technique can simplify the imaging workflows and avoid the impact of external motion compensation signal corruption. Moreover, this motion-resolved aortic imaging technique had another advantage over conventional methods; slicing the 4-way imaging tensor along both diastole and systole phases allowed the aortic vessel strain index and distensibility to be determined, which serves as an important illustration for certain types of aortic diseases (40).

In this work, there was a tradeoff between the scan time and the overall image quality. This is because insufficient imaging data would result in a more undersampled optimization problem to recover the spatial coefficients $\mathbf{U_x}$, as shown in Eqn. (5), which then led to degeneration of the overall image quality. Hence, an optimized protocol needs to balance between the image quality and scan time. Expressly, an optimized scan time means within this specific scan time, enough clinically relevant diagnostic information could be gained; further reduction of the scan time would lead to deterioration of the overall image quality and unconfident diagnoses. Images reconstructed from at least 6 minutes of data produced average scores ≥ 2 for each contrast weighting and no nondiagnostic images (all ≥ 1). One GB image set was scored 1 by reader 1 and two GB image sets were scored 1 by reader 2. The reason for the fair image quality scores was inhomogeneous signal intensities between the ascending and descending aortas, which, however, did not affect the diagnosis of calcifications (black spots). Thereby, the scan time for this proposed technique was finalized as 6 minutes and all quantitative analyses were based on the 6-minute datasets. Measurement results of certain morphological parameters (i.e. lumen and wall area) and functional parameter (i.e. vessel strain index) were in line with those measured through conventional 2D reference techniques, with the lowest intraclass correlation coefficient equals to 0.947 (P < 0.001). The quantitative analysis further illustrates the feasibility of our proposed MT-MACS technique on thoracic aorta.

Our study has some limitations. First, online reconstruction for MT-MACS technique is not available at this stage. Offline reconstruction was performed on a workstation equipped with two 2.70 GHz 12-core Intel Xeon central processing units and 256 GB of random-access memory, with a 110 min median reconstruction time. However, with computing power upgrade and advanced reconstruction methodologies, this challenge may be overcome. Second, a further increase in spatial resolution is necessary. Currently, our spatial resolution

is $1.38 \times 1.38 \times 1.38$ mm^3 isotropic; however, for thoracic aortic imaging, especially aortic vessel wall imaging, a higher resolution is highly desirable to better delineate the aortic vessel and reduce partial volume effects. However, additional scan time is needed to achieve a higher spatial resolution. In the future, additional sources of acceleration, such as deep-learning based super-resolution (41), may be integrated into this technique. Third, feasibility of the proposed technique requires further validation on a larger patient cohort. With multi-dimensional information, our developed method could be used to assess a variety of thoracic aortic diseases, including aortic atherosclerosis, aortic dissection, aortic aneurysm and vasculitis, either pre-contrast or post-contrast. Thus, more patients need to be recruited to further test the sensitivity and specificity of this technique with respect to different types of thoracic aortic diseases.

5. Conclusion

We have demonstrated that the proposed MT-MACS technique provides high-quality, multi-dimensional images for a comprehensive assessment of the thoracic aorta. Technical feasibility of MT-MACS was shown in healthy subjects and patients with thoracic aortic diseases. Further studies in the setting of various thoracic aortic diseases are warranted to validate the clinical utility of this technique.

Supplementary Material

Refer to Web version on PubMed Central for supplementary material.

Acknowledgement

7. Reference

1. François CJ, Carr JC. MRI of the Thoracic Aorta. Cardiology Clinics 2007;25(1):171–184. [PubMed: 17478245]

2. Stanger O, Pepper JR. Surgical Management of Aortic Pathology: Current Fundamentals for the Clinical Management of Aortic Disease: Springer Vienna; 2018.

3. Mendel T, Popow J, Hier DB, Czlonkowska A. Advanced atherosclerosis of the aortic arch is uncommon in ischemic stroke: an autopsy study. Neurological research 2002;24(5):491–494. [PubMed: 12117321]

4. Loebe M, Ren D, proceedings in … R-L. Acute and chronic thoracic aortic disease: surgical considerations. HSR proceedings in … 2012.

5. Dudzinski DM, Isselbacher EM. Diagnosis and Management of Thoracic Aortic Disease. Current Cardiology Reports 2015;17(12):106. [PubMed: 26468124]

6. Katz ES, Konecky N, Tunick PA, Rosenzweig BP, Freedberg RS, Kronzon I. Visualization and identification of the left common carotid and left subclavian arteries: a transesophageal echocardiographic approach. Journal of the American Society of Echocardiography 1996;9(1):58–61. [PubMed: 8679237]

7. Hiratzka LF, Bakris GL, Beckman JA, Bersin RM, Carr VF, Casey DE, Eagle KA, Hermann LK, Isselbacher EM, Kazerooni EA. 2010 ACCF/AHA/AATS/ACR/ASA/SCA/SCAI/SIR/STS/SVM guidelines for the diagnosis and management of patients with thoracic aortic disease. Journal of the American College of Cardiology 2010;55(14):e27–e129. [PubMed: 20359588]

8. Baliyan V, Verdini D, Meyersohn NM. Noninvasive aortic imaging. Cardiovascular Diagnosis and Therapy 2018;8(1).

9. Zhou C, Qiao H, He L, Yuan C, Chen H, Zhang Q, Li R, Wang W, Du F, Li C, Zhao X. Characterization of atherosclerotic disease in thoracic aorta: A 3D, multicontrast vessel wall imaging study. European Journal of Radiology 2016;85(11):2030–2035. [PubMed: 27776656]

10. Holloway BJ, Rosewarne D, Jones RG. Imaging of thoracic aortic disease. The British journal of radiology 2011;84(special_issue_3):S338–S354. [PubMed: 22723539]

11. Beck L, Mohamed AA, Strugnell WE, Bartlett H, Rodriguez V, Hamilton-Craig C, Slaughter RE. MRI measurements of the thoracic aorta and pulmonary artery. Journal of Medical Imaging and Radiation Oncology 2018;62(1):64–71.

12. Krishnam MS, Tomasian A, Malik S, Desphande V, Laub G, Ruehm SG. Image quality and diagnostic accuracy of unenhanced SSFP MR angiography compared with conventional contrast-enhanced MR angiography for the assessment of thoracic aortic diseases. European Radiology 2010;20(6):1311–1320. [PubMed: 20013276]

13. Russo V, Renzulli M, La Palombara C, Fattori R. Congenital diseases of the thoracic aorta. Role of MRI and MRA. European radiology 2006;16(3):676–684. [PubMed: 16249863]

14. Potthast S, Mitsumori L, Stanescu LA, Richardson ML, Branch K, Dubinsky TJ, Maki JH. Measuring aortic diameter with different MR techniques: Comparison of three-dimensional (3D) navigated steady-state free-precession (SSFP), 3D contrast-enhanced magnetic resonance angiography (CE-MRA), 2D T2 black blood, and 2D cine SSFP. Journal of Magnetic Resonance Imaging 2010;31(1):177–184. [PubMed: 20027585]

15. Lanzman RS, Kröpil P, Schmitt P, Freitag S-M, Ringelstein A, Wittsack H Jr, Blondin D. Nonenhanced free-breathing ECG-gated steady-state free precession 3D MR angiography of the renal arteries: comparison between 1.5 T and 3 T. American Journal of Roentgenology 2010;194(3):794–798. [PubMed: 20173162]

16. Roes SD, Westenberg J, Doornbos J, van der Geest RJ, Angelié E, de Roos A, Stuber M. Aortic vessel wall magnetic resonance imaging at 3.0 Tesla: A reproducibility study of respiratory navigator gated free-breathing 3D black blood magnetic resonance imaging. Magnetic Resonance in Medicine 2009;61(1):35–44. [PubMed: 19097222]

17. Mihai G, Chung YC, Merchant A, Simonetti OP, Rajagopalan S. T1-weighted–SPACE dark blood whole body magnetic resonance angiography (DB-WBMRA): Initial experience. Journal of Magnetic Resonance Imaging: An Official Journal of the International Society for Magnetic Resonance in Medicine 2010;31(2):502–509.

18. Wehrum T, Dragonu I, Strecker C, Hennig J, Harloff A. Multi-contrast and three-dimensional assessment of the aortic wall using 3 T MRI. European journal of radiology 2017;91:148–154. [PubMed: 28629561]

19. Tobey DJ, Reynolds TS, Kopchok GE, Donayre CE, Khoynezhad A, White RA. In Vivo Assessment of Ascending and Arch Aortic Compliance. Annals of vascular surgery 2019;57:22–28. [PubMed: 30710630]

20. Lalande A, Khau Van Kien P, Walker P, Zhu L, Legrand L, Claustres M, Jeunemaitre X, Brunotte F, Wolf J-E. Compliance and pulse wave velocity assessed by MRI detect early aortic impairment in young patients with mutation of the smooth muscle myosin heavy chain. Journal of Magnetic Resonance Imaging: An Official Journal of the International Society for Magnetic Resonance in Medicine 2008;28(5):1180–1187.

21. Christodoulou AG, Shaw JL, Nguyen C, Yang Q, Xie Y, Wang N, Li D. Magnetic resonance multitasking for motion-resolved quantitative cardiovascular imaging. Nature biomedical engineering 2018;2(4):215.

22. Shaw JL, Yang Q, Zhou Z, Deng Z, Nguyen C, Li D, Christodoulou AG. Free-breathing, non-ECG, continuous myocardial T1 mapping with cardiovascular magnetic resonance multitasking. Magnetic resonance in medicine 2019;81(4):2450–2463. [PubMed: 30450749]

23. Liang Z-P. Spatiotemporal imagingwith partially separable functions. 2007 IEEE p 988–991.

24. Kolda TG, Bader BW. Tensor decompositions and applications. SIAM review 2009;51(3):455–500.

25. Christodoulou AG, Redler G, Clifford B, Liang Z-P, Halpern HJ, Epel B. Fast dynamic electron paramagnetic resonance (EPR) oxygen imaging using low-rank tensors. Journal of Magnetic Resonance 2016;270:176–182. [PubMed: 27498337]

26. He J, Liu Q, Christodoulou AG, Ma C, Lam F, Liang Z-P. Accelerated high-dimensional MR imaging with sparse sampling using low-rank tensors. IEEE transactions on medical imaging 2016;35(9):2119–2129. [PubMed: 27093543]

27. Trzasko JD, Manduca A. A unified tensor regression framework for calibrationless dynamic, multi-channel MRI reconstruction. 2013.

28. Bustin A, Lima da Cruz G, Jaubert O, Lopez K, Botnar RM, Prieto C. High-dimensionality undersampled patch-based reconstruction (HD-PROST) for accelerated multi-contrast MRI. Magnetic resonance in medicine 2019;81(6):3705–3719. [PubMed: 30834594]

29. Yaman B, Weingärtner S, Kargas N, Sidiropoulos ND, Akçakaya M. Low-Rank Tensor Models for Improved Multi-Dimensional MRI: Application to Dynamic Cardiac T1 Mapping. IEEE Transactions on Computational Imaging 2019.

30. Wang N, Christodoulou AG, Xie Y, Wang Z, Deng Z, Zhou B, Lee S, Fan Z, Chang H, Yu W. Quantitative 3D dynamic contrast-enhanced (DCE) MR imaging of carotid vessel wall by fast T1 mapping using Multitasking. Magnetic resonance in medicine 2019;81(4):2302–2314. [PubMed: 30368891]

31. Ma S, Nguyen CT, Han F, Wang N, Deng Z, Binesh N, Moser FG, Christodoulou AG, Li D. Three-dimensional simultaneous brain T1, T2, and ADC mapping with MR Multitasking. Magnetic resonance in medicine 2019.

32. Liu CY, Bley TA, Wieben O, Brittain JH, Reeder SB. Flow-independent T2-prepared inversion recovery black-blood MR imaging. Journal of Magnetic Resonance Imaging 2010;31(1):248–254. [PubMed: 20027595]

33. Xie J, Bi X, Fan Z, Bhat H, Shah S, Zuehlsdorff S, Li D. 3D flow-independent peripheral vessel wall imaging using T2-prepared phase-sensitive inversion-recovery steady-state free precession. Journal of Magnetic Resonance Imaging 2010;32(2):399–408. [PubMed: 20677269]

34. Godia EC, Madhok R, Pittman J, Trocio S, Ramas R, Cabral D, Sacco RL, Rundek T. Carotid artery distensibility: a reliability study. Journal of Ultrasound in Medicine 2007;26(9):1157–1165. [PubMed: 17715309]

35. Amano Y, Takahama K, Kumita S. Non–contrast-enhanced MR angiography of the thoracic aorta using cardiac and navigator-gated magnetization-prepared three-dimensional steady-state free precession. Journal of Magnetic Resonance Imaging: An Official Journal of the International Society for Magnetic Resonance in Medicine 2008;27(3):504–509.

36. Koktzoglou I Gray blood magnetic resonance for carotid wall imaging and visualization of deep-seated and superficial vascular calcifications. Magnetic Resonance in Medicine 2013;70(1):75–85. [PubMed: 22887594]

37. Miura T, Matsukawa N, Sakurai K, Katano H, Ueki Y, Okita K, Yamada K, Ojika K. Plaque vulnerability in internal carotid arteries with positive remodeling. Cerebrovascular diseases extra 2011;1(1):54–65. [PubMed: 22566983]

38. Harloff A, Brendecke SM, Simon J, Assefa D, Wallis W, Helbing T, Weber J, Frydrychowicz A, Vach W, Weiller C. 3D MRI provides improved visualization and detection of aortic arch plaques compared to transesophageal echocardiography. Journal of Magnetic Resonance Imaging 2012;36(3):604–611. [PubMed: 22552960]

39. Fan Z, Yu W, Xie Y, Dong L, Yang L, Wang Z, Conte AH, Bi X, An J, Zhang T. Multi-contrast atherosclerosis characterization (MATCH) of carotid plaque with a single 5-min scan: technical development and clinical feasibility. Journal of Cardiovascular Magnetic Resonance 2014;16(1):53. [PubMed: 25184808]

40. Redheuil A, Wu CO, Kachenoura N, Ohyama Y, Yan RT, Bertoni AG, Hundley GW, Duprez DA, Jacobs DR, Daniels LB. Proximal aortic distensibility is an independent predictor of all-cause mortality and incident CV events: the MESA study. Journal of the American College of Cardiology 2014;64(24):2619–2629. [PubMed: 25524341]
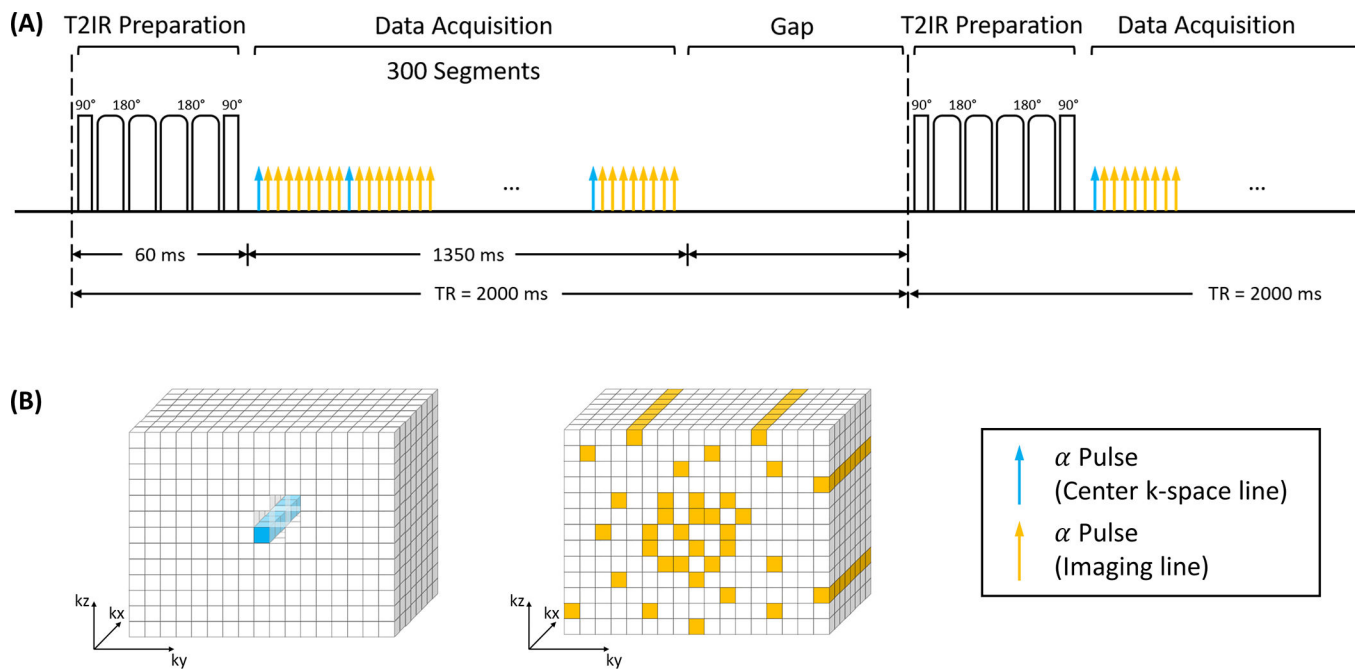
41. Chen Y, Shi F, Christodoulou AG, Xie Y, Zhou Z, Li D. Efficient and accurate MRI super-resolution using a generative adversarial network and 3D multi-level densely connected network. 2018 Springer p 91–99.

Figure 1.
Pulse sequence diagram for MT-MACS technique and corresponding k-space sampling pattern. **(A)** Nonselective T2-preparation inversion recovery (T2-IR) pulses were applied every TR followed by continuous FLASH readout alpha pulses. One k-space line was collected every alpha pulse. After each blue arrow, an auxiliary line was acquired every 9 lines as the low-rank tensor subspace training data. Data acquisition module contained 300 readout segments followed by a short gap of fixed duration until the next T2-IR preparation pulse. **(B)** Simplified illustration of k-space sampling strategy. The auxiliary data was collected at the k-space center. Cartesian sampling with randomized reordering with a variable-density Gaussian distribution in ky and kz directions was adopted in this sequence.
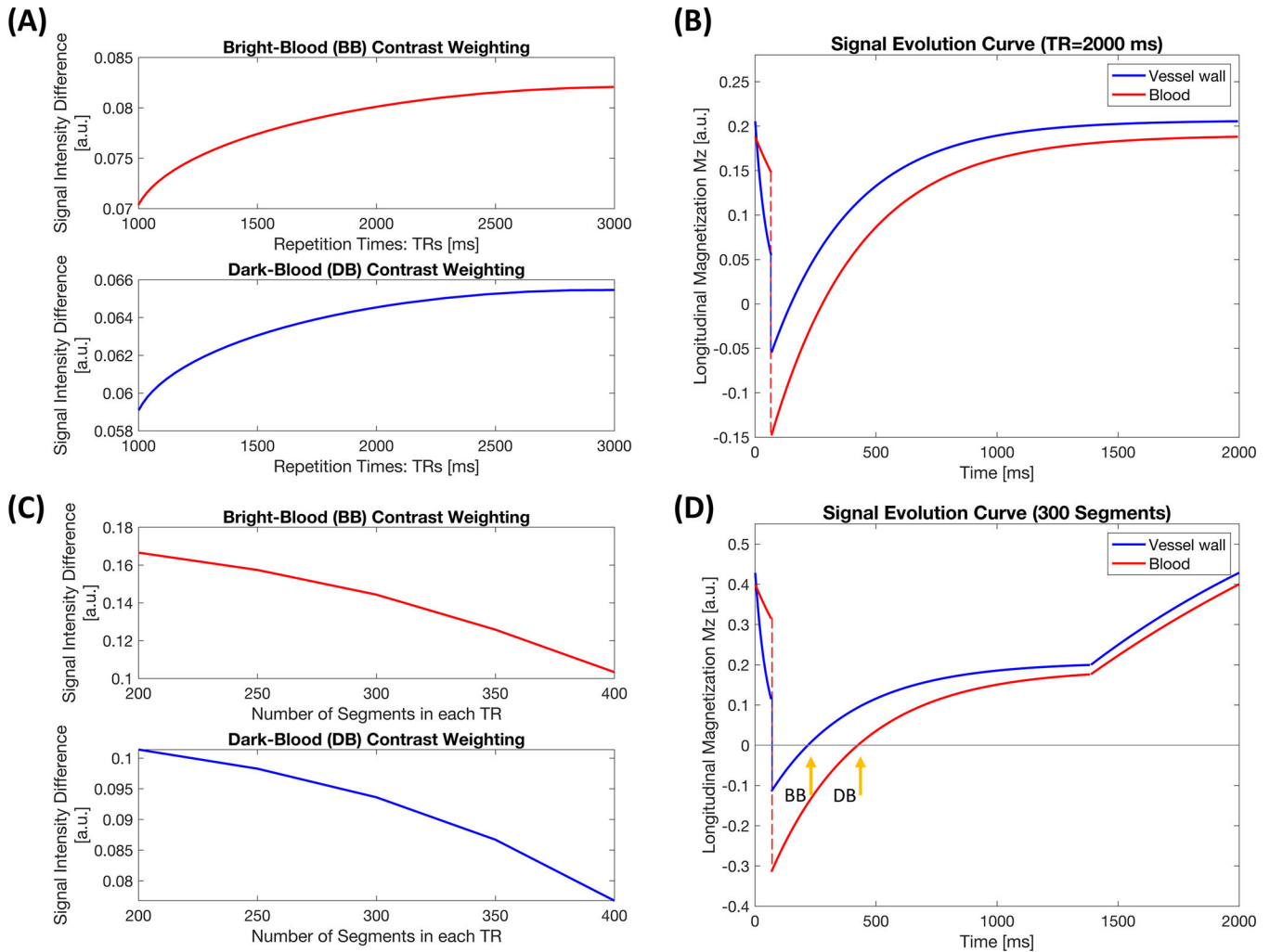
Figure 2.
Simulation results. **(A)** Curve of lumen-wall contrast with respect to bright-blood and dark-blood contrast weightings against various TRs with no gap until the next T2-preparation inversion recovery (T2-IR) prepared pulse. **(B)** Signal evolution curves of the aortic vessel wall and lumen blood with a 2000-ms repetition time. **(C)** Curve of lumen-wall signal difference against numbers of segments during a single readout block with TR = 2000 ms. **(D)** Signal evolution curves of the aortic vessel wall and lumen blood with 300 readout segments followed by a 600-ms gap until the next preparation pulse, under the circumstance of TR = 2000 ms. Two representative time points were selected for bright-blood and dark-blood contrast weightings during the simulation study.
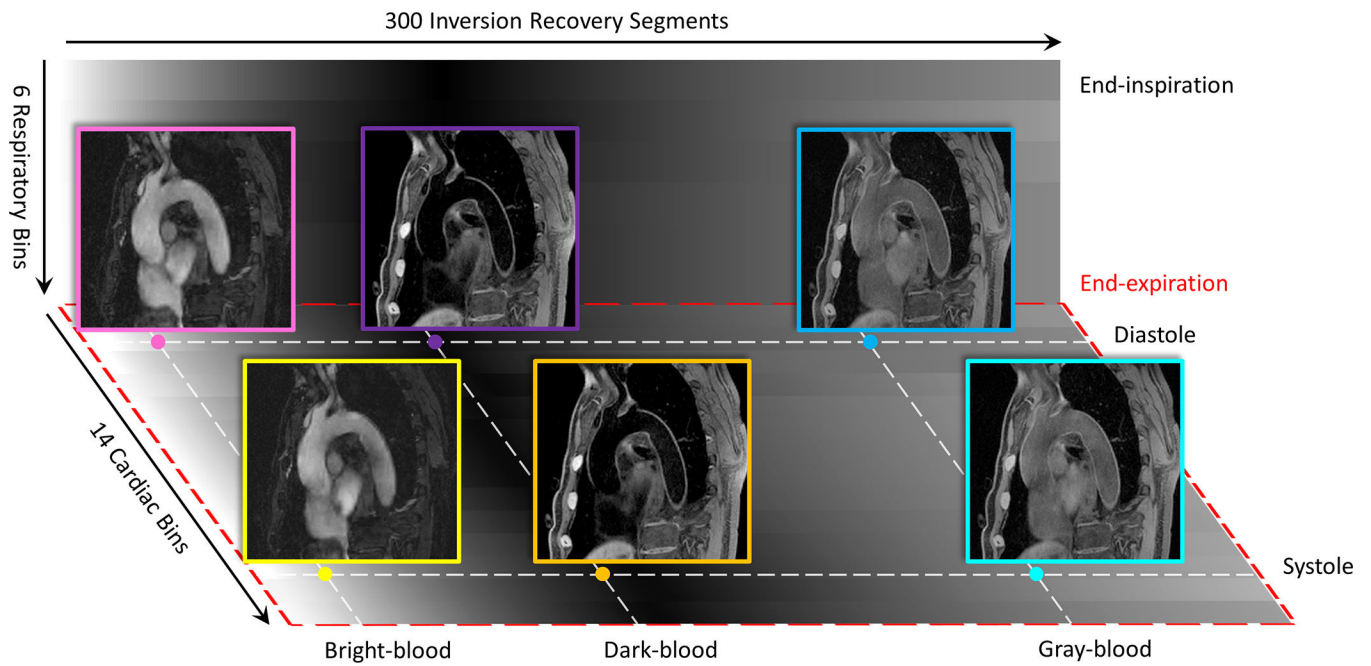
Figure 3.
Illustration of different time dimensions for MT-MACS, namely, cardiac pulsation, respiration and T2-prepared inversion recovery dimensions. For phase-resolved imaging, MT-MACS divides cardiac motion and respiratory movement into 14 and 6 bins, respectively. Within each inversion recovery period, MT-MACS contains 300 readout segments which can generate 300 various contrast weightings. 3 typical contrast weightings (i.e. bright-blood [BB], dark-blood [DB] and gray-blood [GB]) are picked out for multi-contrast assessment.

(A)

(B)
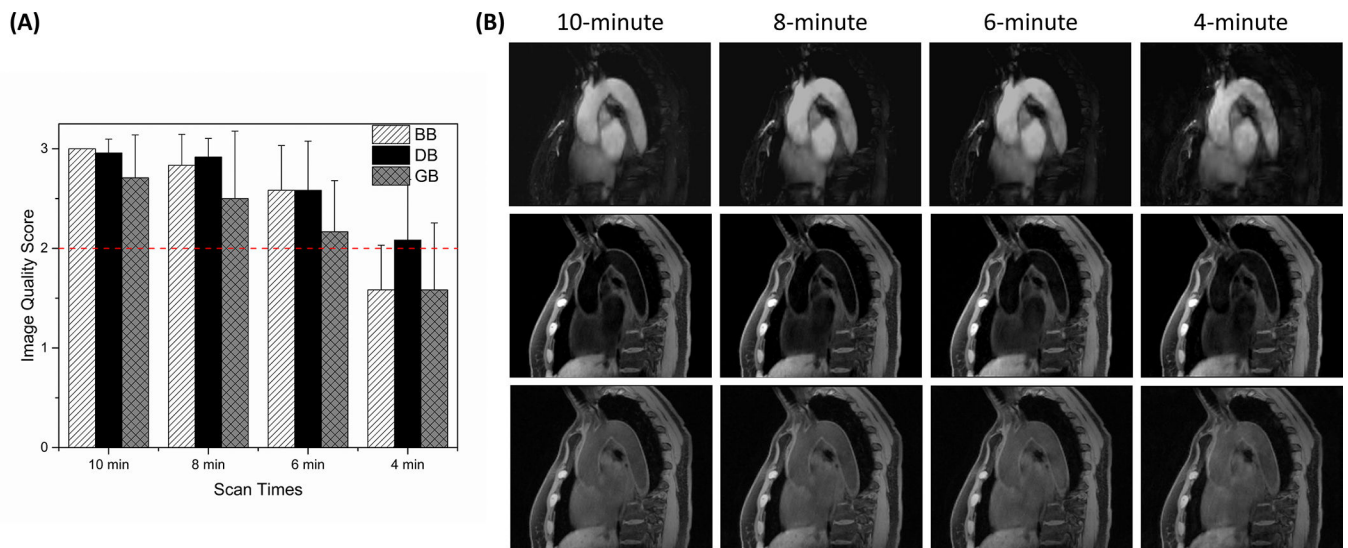
Figure 4.
Qualitative analysis results. **(A)** Average values of the overall image quality scores given by two readers and the standard deviations over all 12 subjects for each image contrast within each scan time category. The red dotted line denotes the mean diagnostic level (score 2), and the optimal scan time was determined as the shortest one that generated average scores over all subjects for each image contrast above this level. For BB and GB images reconstructed using a 4-minute dataset, the average image quality scores were less than 2, which were not enough for clinicians and radiologists to obtain clinically related information. **(B)** One of the empirical studies illustrated the tradeoff between the overall image quality and scan time. Further cut down the scan time to 4 minutes will lead to severe deterioration of the overall image quality. BB: bright-blood; DB: dark-blood; GB: gray-blood.
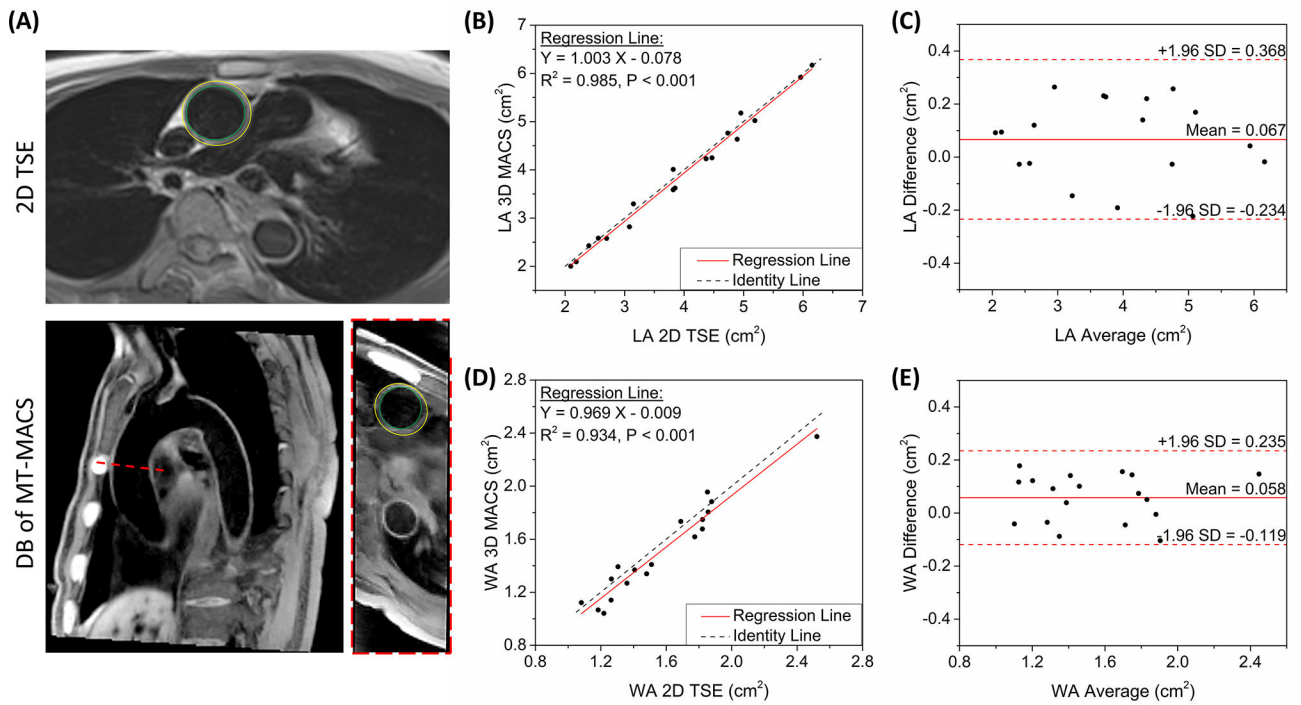
Figure 5.
Quantification of morphological parameters of aortic vessels. **(A)** Graphic illustration of measuring the lumen area and wall area in healthy subjects. The inner and outer contours were manually traced on both 2D TSE images and dark-blood images of MT-MACS. Both the slice position and slice thickness were matched during the measurements. **(B)(D)** Comparison of lumen and wall area measurement, respectively, using the proposed MT-MACS and a convention 2D TSE reference. Black dotted lines represent identity line (Y = X), while solid red lines stand for regression of the results from these 2 methods. The intraclass correlation coefficients (ICC) for LA and WA measurements were 0.993 (P < 0.001) and 0.969 (P < 0.001), respectively. **(C)(E)** Bland-Altman plots comparing measurement results acquired by these two imaging techniques. Solid red lines and dashed red lines indicate the means and standard deviation of LA and WA values between different methods.
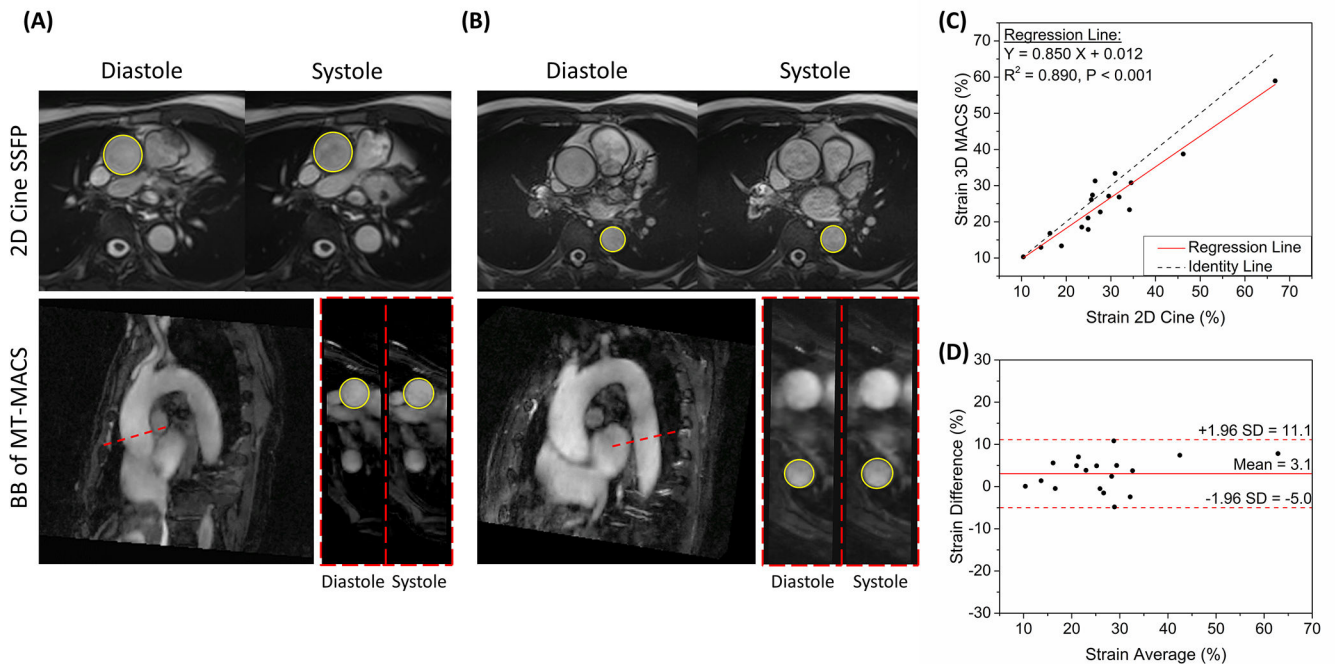
Figure 6.
Quantification of the functional parameter of aortic vessels. **(A)(B)** Graphic illustration of measuring the diastolic and systolic lumen area of both the ascending and descending aortas in healthy subjects. The lumen boundaries were manually traced on 2D cine SSFP images and bright-blood images of MT-MACS. Both the slice position and slice thickness were matched during the measurements. **(C)** Comparison of aortic vessel strain measurement, using the proposed MT-MACS and a convention 2D cine reference. The black dotted line represents identity line $(Y = X)$, while the solid red line stands for regression of the results from these 2 methods. The intraclass correlation coefficient (ICC) was 0.947 ($P < 0.001$). **(D)** Bland-Altman plots comparing measurement results acquired by these two imaging techniques. Solid red line and dashed red lines indicate the mean and standard deviation of strain values between different methods.
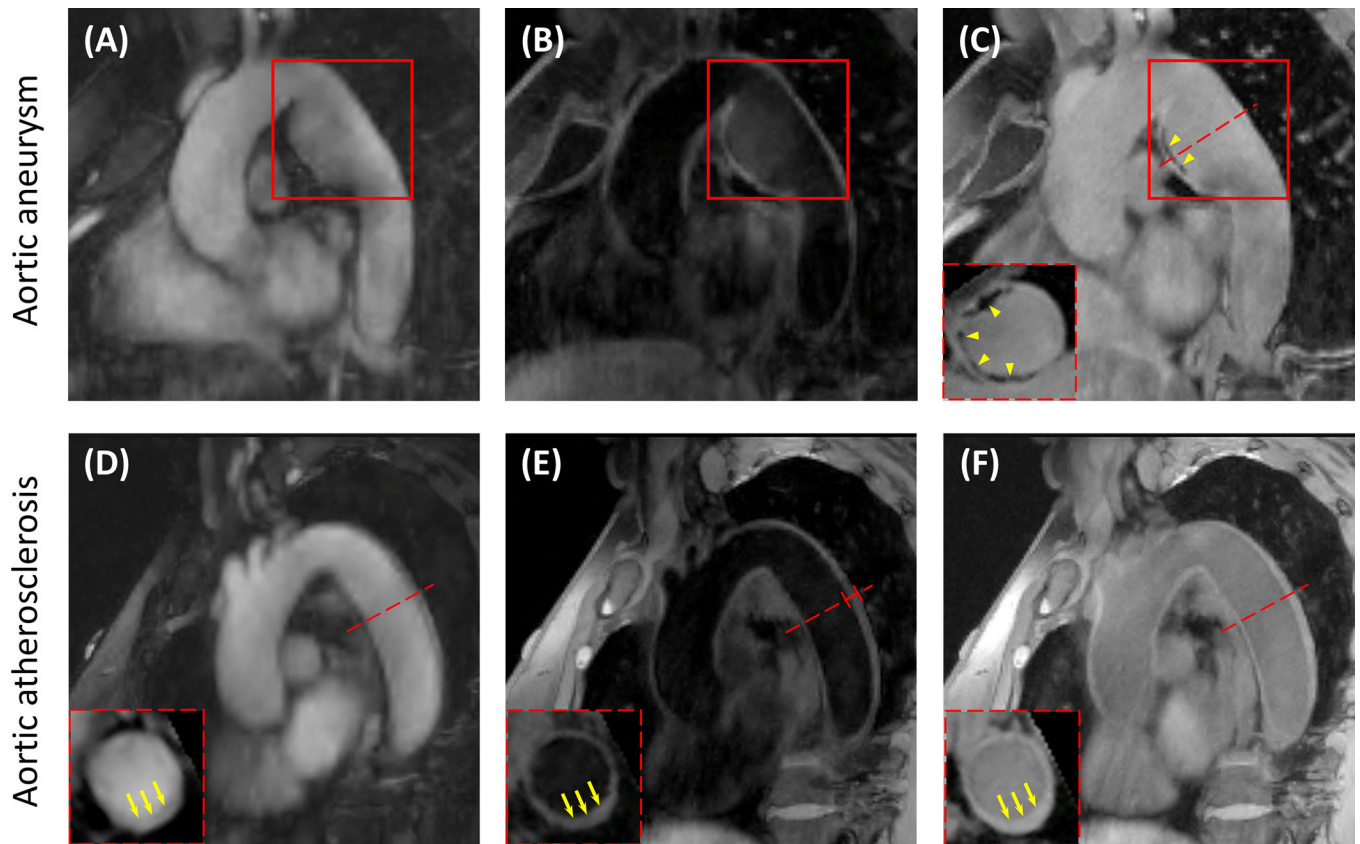
Figure 7.

Images from two patients with aortic aneurysm and aortic atherosclerosis, respectively. **(A)** Bright-blood, **(B)** dark-blood and **(C)** gray-blood contrast weightings from a 38-year-old female patient with aortic aneurysm. Aneurysm in the patient's descending aorta was depicted (red boxes). Calcifications were also identified by GB imaging and the circumferential extent of the abnormalities could be seen through short-axis views (yellow arrowheads). **(D)** Bright-blood, **(E)** dark-blood and **(F)** gray-blood images acquired from a 71-year-old female patient with aortic atherosclerosis. Increased aortic wall thickness (4.491 mm) was marked out in red on the oblique sagittal dark-blood image. The severe thickening of the vessel wall could be clearly identified through the short-axis views of the DB and GB imaging, which were pointed out by the yellow arrows.